Evidence for auroral influence on Jupiter's nitrogen and oxygen chemistry revealed by ALMA

Check for updates

T. Cavalié [1,2] ✉, L. Rezac [3], R. Moreno [2], E. Lellouch [2], T. Fouchet [2], B. Benmahi[1], T. K. Greathouse[4], J. A. Sinclair [5], V. Hue[4], P. Hartogh[3], M. Dobrijevic[1], N. Carrasco [6] & Z. Perrin[6]

The localized delivery of new long-lived species to Jupiter's stratosphere by comet Shoemaker–Levy 9 in 1994 opened a window to constrain Jovian chemistry and dynamics by monitoring the evolution of their vertical and horizontal distributions. However, the spatial distributions of CO and HCN, two of these long-lived species, had never been jointly observed at high latitudinal resolution. Atacama large millimeter/submillimeter array observations of HCN and CO in March 2017 show that CO was meridionally uniform and restricted to pressures lower than 3 ± 1 mbar. HCN shared a similar vertical distribution in the low- to mid-latitudes, but was depleted at pressures between 2^{+2}_{-1} and $0.04^{+0.07}_{-0.03}$ mbar in the aurora and surrounding regions, resulting in a drop by two orders of magnitude in column density. We propose that heterogeneous chemistry bonds HCN on large aurora-produced aerosols at these pressures in the Jovian auroral regions causing the observed depletion.

Jupiter is an archetype for gas giants (in the Solar System and in extrasolar systems). Like the other giants in the Solar System, it is a fast rotator (9.9 h period). The sheer size and angular speed induce a very complex atmospheric structure, circulation and meteorological system such that the dynamics and chemistry at work in Jupiter's atmosphere are still poorly understood.

Mainly composed of hydrogen and helium, giant planets also contain 0.2–4% methane. Methane's photolysis at high altitude initiates the production of more complex hydrocarbons[1]. Giant planets also capture external material, in the form of infalling comets, interplanetary dust or gas and grains from their ring and satellite systems[2], contributing to enhance the complexity of the chemistry of their atmospheres. While one-dimensional (1D) photochemical models generally succeed in explaining the disc-averaged abundances of these species[1], no model has yet managed to reproduce the meridional distributions and the temporal evolution of their hydrocarbons and other trace species (for example, ref. 3).

A rare event on Jupiter can help us better constrain both chemistry and dynamics in Jupiter's atmosphere. July 1994 saw the first extraterrestrial collision in the Solar System witnessed from Earth with multispectral observations. The 21 fragments of comet Shoemaker–Levy 9 (SL9) spectacularly impacted Jupiter in its southern hemisphere near 44° S (ref. 4), increased its temperature locally[5,6] and left the planet with visible dark scars for weeks (for example, refs. 7,8). Even more notable in the long term, the SL9 impacts produced a series of species previously undetected in the stratosphere, such as CO, HCN, CS, H_2O and CO_2 (refs. 9–11), probably from shock chemistry during the impacts[12], except CO_2 that probably formed subsequently from atmospheric photochemistry[13]. These species were deposited at roughly 0.1 mbar during the splashback of the impact plumes[14,15], and subsequently spread in

[1]University of Bordeaux, CNRS, LAB, UMR 5804, Pessac, France. [2]LESIA, Paris Observatory, University of PSL, CNRS, Sorbonne University, University of Paris, Meudon, France. [3]Max-Planck-Institute for Solar System Research, Göttingen, Germany. [4]Southwest Research Institute, San Antonio, TX, USA. [5]Jet Propulsion Laboratory, California Institute of Technology, Pasadena, CA, USA. [6]LATMOS, CNRS, UVSQ University of Paris-Saclay, Sorbonne University, Guyancourt, France. ✉e-mail: thibault.cavalie@u-bordeaux.fr

Jupiter's stratosphere. Whereas they contaminated all longitudes at the impact site latitude within roughly 1 year (ref. [16]), the meridional and vertical diffusion occurred on longer timescales[15], predicting that meridional eddy diffusion would require more than a decade to see abundances uniformly mixed. This was confirmed by observations of HCN and CO_2 in 1995 and 2000 (refs. [17,18]) and the long-term monitoring of the H_2O vertical distribution[19,20]. Given that CO, HCN, CS and H_2O have sufficiently long chemical lifetimes (more than 10 years), their deposition by SL9 in 1994 offers us a unique opportunity to study the temporal evolution of their distributions over several years and now decades. This is a powerful tool to better understand the chemistry and dynamics of Jupiter's stratosphere.

CO, HCN and CS have been monitored ever since the SL9 impacts (for example, ref. [15]), and their distributions were mapped until 1998 with a moderate spatial resolution of one-third to one-quarter of the planet diameter. Further monitoring over the following decade consistently showed a slow decrease of their disc-averaged masses, with decay factors ranging from 5 to 15 between 1998 and 2006 for the different species. Despite the slow decrease of their abundances, CO, HCN and CS are stable enough to use as dynamical tracers in the Jovian atmosphere, using their vertical and latitudinal distributions. Based on observations over 1994–1997 with the IRAM-30m[15] and the IRTF[17], the first estimates on latitudinal eddy mixing were obtained. Lellouch et al.[18] revealed that, in addition to a large S–N hemispheric asymmetry caused by the slow diffusion from the impact sites toward northern latitudes, HCN showed an abrupt decrease southwards of 45° S and northwards of 50° N that was interpreted as a 'dynamical barrier' isolating the high latitudes from other latitudes.

Most of all, CO_2, observed simultaneously with HCN by Cassini, revealed a different distribution from HCN, peaking at the south pole instead[18]. The difference is difficult to understand as CO_2 is thought to be a daughter molecule of CO (from CO + OH → CO_2 + H, where OH is produced from H_2O)[13], which was produced by the SL9 impacts, similar to HCN. Lellouch et al.[18] explored models in which the CO_2 polar excess was associated with the conversion of precipitating oxygen-bearing material to CO_2, but did not find this to be a promising scenario and they also investigated various horizontal transport models combining latitudinal advection and strongly latitude-dependent eddy mixing and tentatively concluded that the HCN and CO_2 were affected by meridional transport in opposite directions (equatorwards and polewards, respectively), indicating that the two species resided at different atmospheric levels. The conclusions were, however, strongly hampered by the lack of information on the behaviour of CO.

Observations

We used ALMA (Atacama large millimeter/submillimeter array) and Gemini/TEXES observations[21–23] to retrieve the spatial distribution of HCN and CO in Jupiter's stratosphere to better understand their temporal evolution. The ALMA observations consist of high signal-to-noise ratio maps of the HCN (4-3) and CO (3-2) spectral emissions and were recorded on 22 March 2017. A sample of spectra is shown in Fig. 1. The latitudinal resolution was roughly 2° at low latitudes and the spectral resolving power 3×10^6. The Gemini/TEXES observations of the CH_4 band at 7.8 μm were recorded on 14, 16 and 20 March 2017 in ref. [22] for the low-to-mid-latitudes and on 17–19 March 2017 in ref. [23] for the high latitudes. These were used to retrieve the temperature field between 1 μbar and 50 mbar with uncertainties less than 2 K. The northern polar region was mapped on 17 and 19 March, while the southern polar region was only mapped on 18 March. We filled latitude and longitude coverage gaps by interpolating between the data points (Extended Data Fig. 1). We used the combination of temperature maps obtained nearly simultaneously to the ALMA observations, a forward radiative transfer modelling and a retrieval algorithm (Methods) to retrieve the vertical profiles of HCN and CO as a function of latitude from spectra observed at the limb of Jupiter (Extended Data Fig. 2). These profiles are
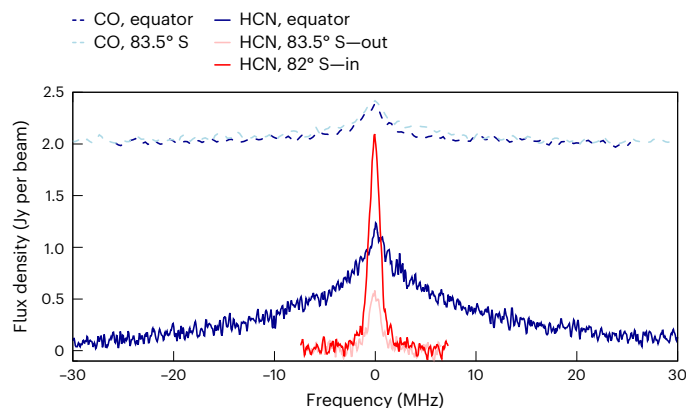
Fig. 1 | Sample of HCN and CO spectra observed with ALMA in Jupiter on 22 March 2017. Their corresponding latitude on Jupiter is given ('in' stands for inside the aurora and is on the 350 W limb, and 'out' stands for outside the aurora and is on the 170 W limb). All spectra have been centred around their central frequency for an easier comparison and the CO spectra have been shifted by 2 Jy per beam.
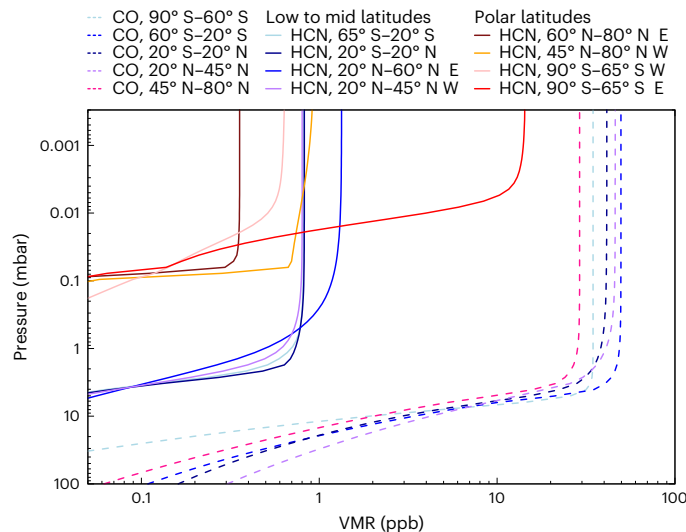

Fig. 2 | HCN and CO volume mixing ratio vertical profiles in Jupiter's stratosphere. The HCN (solid lines) and CO (dashed lines) retrieved profiles have been averaged by latitude bins for clarity. For HCN, we differentiate profiles seen on each limb for some particular latitude bins. E stands for the eastern limb (350 W longitude) and W for the western one (170 W longitude). The vertical range corresponds to the range of vertical sensitivity. VMR, volume mixing ratio.

parametrized with three independent numbers, which essentially mirror the fact that the line amplitude depends on the mole fraction in the upper stratosphere and that the whole lineshape controls the pressure above which the mole fraction drops and the slope of the decrease. The vertical profile retrievals have a very limited sensitivity to the temperature uncertainties (less than 1%), because the lines are not optically thick (that is, $\tau = 0.2$ for CO, 0.4 for HCN at high latitudes and 1.6 for HCN in the low- to mid-latitudes).

The spatial distribution of CO and HCN

A sample of CO vertical profiles averaged per latitude bins is shown in Fig. 2. The whole set of retrieved profiles is shown in Extended Data Fig. 3 and we took these profiles to compute the column density as a function of latitude. The meridional distribution of CO is shown in Fig. 3. It essentially shows that CO was rather uniformly mixed as a
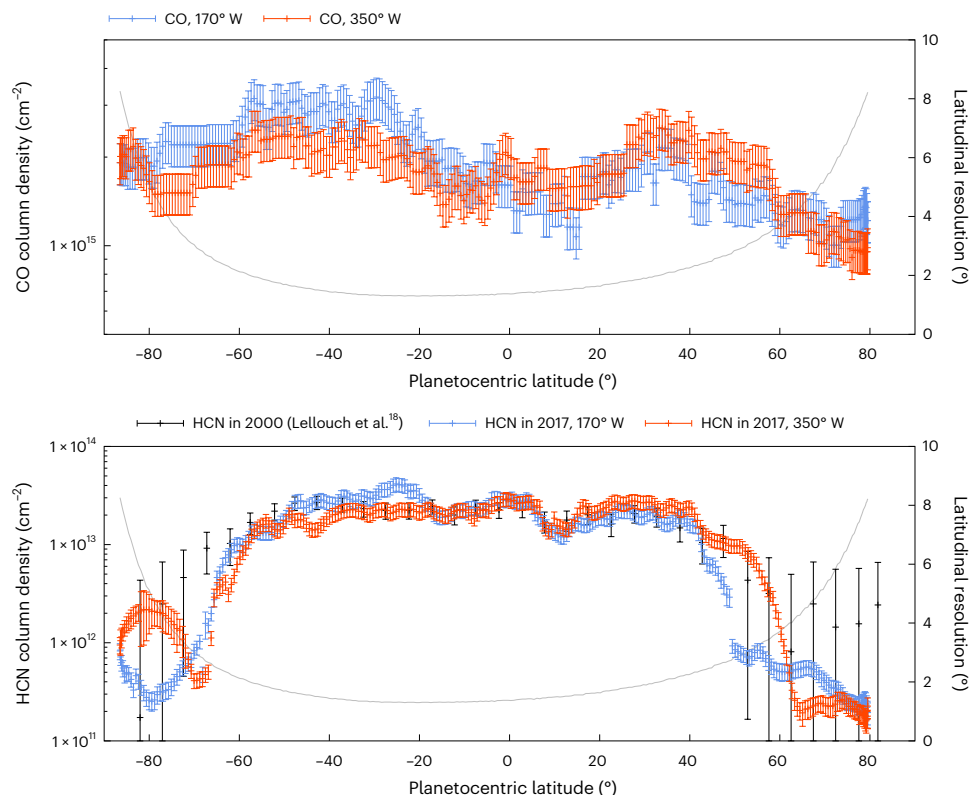
Fig. 3 | CO (top) and HCN (bottom) column densities as a function of planetocentric latitude at the longitudes of the two observed limbs. CO is shown in the top panel and HCN in the bottom one, with mean values and $1-\sigma$ error bars. The HCN measurements (mean values and $1-\sigma$ error bars) from ref. 18 are plotted for comparison and the data values have been rescaled by dividing them by 120. The latitudinal resolution of the ALMA observations is shown with the grey line.

function of latitude in Jupiter's stratosphere as of March 2017. We can then put a lower limit on meridional mixing, K_{yy}. For CO to populate all latitudes starting from the impact latitude in maximum $\Delta t = 22.5$ years, that is, the time elapsed between the SL9 impacts and our observations, it requires $K_{yy} \approx \frac{L^2}{\Delta t} \geq 3.7 \times 10^{11}$ cm^2 s^{-1} around mbar pressures, with L being the distance from 44° S to the north pole. This is consistent with the values derived by refs. 13,15,18. With the three-parameter fit profile, we find a CO mole fraction of 41 ± 12 ppb ($1-\sigma$ uncertainty) at pressures lower than an average cut-off of 3 ± 1 mbar. The resulting meridionally uniform CO column density is $1.86 \pm 0.52 \times 10^{15}$ cm^{-2}. The total mass of SL9-derived CO is then $5.47 \pm 0.26 \times 10^{13}$ g, which corresponds to a loss factor of 9 ± 3 since 1995–1998 (ref. 15).

The vertical distribution of HCN shows important variability as seen in Fig. 2. This variability does not only depend on latitude, as already known from post-SL9 collision observations[17,18], but also on longitude in the polar domains as demonstrated here by the column density meridional profiles on each limb (Fig. 3). It is uniform from roughly 55° S to 40° N with a value of $22.6 \pm 5.7 \times 10^{12}$ cm^{-2}, which is two orders of magnitude lower than that measured 6.5 years after the SL9 impacts in ref. 18. In this latitudinal range, we find an HCN mole fraction of 0.9 ± 0.5 ppb ($1-\sigma$ uncertainty) at pressures lower than an average cut-off of 2^{+2}_{-1} mbar. The variability seen in the HCN column density, not only on each limb, but also between the eastern and western limbs (at 350 W and 170 W longitude, respectively), being caused by the continuum subtraction performed at the data reduction stage. It is also true for CO at all latitudes. This subtraction is performed using a uniform disc model that does not perfectly fit the zone and/or belt structure of Jupiter's continuum. The line-to-continuum ratio (and thus the retrieved value of the HCN mole fraction at high altitude) is consequently altered up to 30%. On the other hand, the pressure level remains

unaffected. We find a similar structure in the variability of the CO column density profile in this latitudinal range and it is thus also not a real feature. At latitudes southwards of roughly 70° S, northwards of 50° N on the 170 W limb and northwards of 65° N on the 350 W limb, the HCN column density drops by a factor of 25–100 with respect to the low- to mid-latitudes. This drop is caused by a depletion of HCN at millibar pressures: the HCN profile is cut-off at a pressure higher than $0.04^{+0.07}_{-0.03}$ mbar in these regions, translating into much narrower lines compared to those seen in the low- to mid-latitudes (Fig. 1). In addition, there is an asymmetry in column density between the 350 W and 170 W limbs in the 45° N–65° N latitude range. Also, on the 350 W limb, between 75° S and 85° S, the HCN abundance above the cut-off altitude is notably higher than at other southern polar latitudes. We will discuss these asymmetries in the next two sections. Integrating the HCN column density meridional profile, we find a total mass of $5.0 \pm 0.1 \times 10^{11}$ g. This corresponds to a loss factor of 50 ± 30 when compared with the 1995–1998 period[15], or 120 ± 35 when compared with the value derived in 2000 from the Cassini flyby data[18]. The HCN column density was indeed higher in 2000 compared to 1995–1998, probably resulting from secondary production of HCN from NH$_3$ following the comet impacts[18].

HCN at high latitudes

In Fig. 4, we compare the column density on the limb with the statistical average of the ultraviolet (UV) emission of the auroras[24] at the time of our observations, and we find that a first HCN depleted region lies in the latitude domain occupied by the southern auroral region. Although the geometry was less favourable at the time of the observations with the northern auroral oval just rising over the 170 W limb, there is a similar correlation between a second HCN depleted region
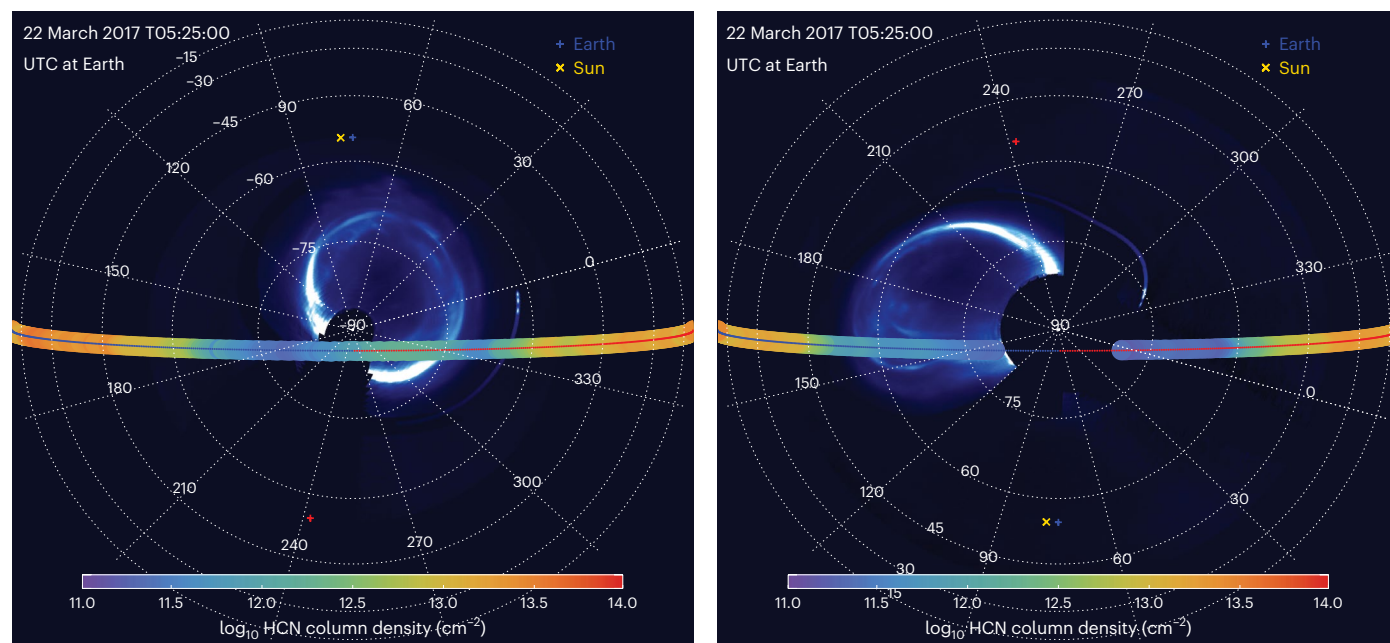
Fig. 4 | Polar projections of the HCN column density. The decimal logarithm of the HCN column density in cm^{-2} is represented according to the observation geometry with ALMA. The solid line in the middle of the column density strip is blue for the western limb and red for the eastern limb. The two panels show the correlation between the HCN depleted region and location of the statistical average of the UV emission of Jupiter's auroras[24]. While the southern aurora (left panel) was clearly in the field, the northern aurora (right panel) was rising on the northwest limb. The former highlights the variability of the HCN column density over southern polar and auroral regions. The model in ref. 24 used observations from multiple Hubble Space Telescope visits. Because of the observation geometrical constraints from Hubble Space Telescope, not all Jovian longitudes were covered, which resulted in the longitudinal gap seen in both panels. The latitudinal resolution of the ALMA measurements ranges from 4° to 8° northwards of 60° N and southwards of 80° S along the limb. Observation date is given in UTC at Earth, where UTC stands for Coordinated Universal Time.

in the north with the northern auroral region. The asymmetry seen between the northwestern and northeastern latitudes at which the HCN column density drops (Fig. 3) is reminiscent of the tilted position of the more extended northern aurora. The northern and southern HCN depletions seem therefore to be related to the auroras. Because CO and HCN reside at similar altitude levels in the low- to mid-latitudes, they must be subject to the same circulation regime and should share the same meridional distribution. The fact that HCN is clearly depleted in the auroral regions between 0.04 and 3 mbar while CO is not can therefore not be caused by a dynamical barrier that would prevent species located in the mid-latitudes to be transported to higher latitudes. Instead, it requires an efficient chemical loss mechanism specific to HCN at the location of the auroras of Jupiter and at pressures of roughly 0.1 mbar and higher. Energetic electrons are known to precipitate from the magnetosphere down to the upper stratosphere in Jupiter's auroras and they could destroy HCN. However, we dismiss this possibility because magnetospheric electrons do not penetrate down to mbar pressures in the auroras[25,26]. Consequently, they cannot explain the HCN depletion at pressures higher than 0.1 bar.

A more promising possibility is heterogeneous chemistry with organic aerosols produced in the auroras. For Titan's atmosphere, ref. 27 proposed that the loss of HCN to solid haze material is an important sink of nitrogen. This idea was extended by Lara et al.[28] and later Vinatier et al.[29], who showed that introducing a sink term for HCN, representing incorporation into the haze, allowed photochemical model results to better match observations of Titan's HCN and hydrocarbons simultaneously. More recently, Perrin et al.[30] have demonstrated that HCN bonds efficiently on organic aerosols produced in laboratory experiments under Titan atmospheric conditions when the aerosols reach a given mass and abundance threshold. The conditions under which these experiments were conducted lead to ion-neutral chemistry initiated by a plasma discharge that are comparable to auroral

conditions. Besides, enhanced efficiency in C_2 hydrocarbon production has been observed in the Jovian auroras by Sinclair et al.[31], as initially predicted by models by Wong et al.[32]. These hydrocarbons are precursors for higher order hydrocarbons in Jupiter's auroral region. Growing carbon chains eventually lead to the formation of benzene (observed by, for example, Bézard et al.[33]) and eventually polycyclic aromatic hydrocarbons in the 10^{-3}–10^{-1} mbar pressure range according to Wong et al.[34]. Combining the results of the latter chemistry model with an aerosol microphysical model, Friedson et al.[35] predicted that, among polycyclic aromatic hydrocarbons, pyrene first condenses when the pressure exceeds 0.1 mbar and serves as condensation nuclei for phenanthrene and naphthalene. The resulting particles then sediment in the auroral regions as they continue to grow, reaching radii of roughly 0.1 μm and eventually leading to the formation of larger aerosols between 0.1 and 1 mbar. Our observations demonstrate that HCN is removed from the gas phase at pressures higher than roughly 0.1 mbar in the auroras where Friedson et al.[35] predict that roughly 0.1 μm aerosols start to form. These aerosols would continue to grow to micrometre sizes and sediment inside the auroras, eventually spreading out to other latitudes and longitudes where the auroral winds break (between 0.1 and a few mbar[21]) and accumulating in the middle stratosphere where they were mapped by Zhang et al.[36]. The smaller and higher altitude aerosols, which we presume are responsible for the HCN depletion, remain to be observed. The fact that HCN is removed not only from the interior of the main auroral ovals, but also from the surrounding polar latitudes and longitudes, remains to be explained. In the framework of our interpretation, HCN is no longer depleted between 0.04 and 3 mbar outside the high latitude region, because aerosols are located at too-high pressures[36].

HCN interior of the southern auroral oval

A local increase of the column density can be spotted on the 350 W limb at the location of the southern aurora: it can be seen in the data

shown in red in Fig. 3 in the range 75° S–85° S, which also corresponds to the vertical profile plotted in red in Fig. 2 and to the light blue region interior of the aurora in the polar projection of Fig. 4 (left). It reflects an increase in the line emission interior of the southern auroral oval, a region where auroral heating at mbar and sub-mbar levels is known to be important[31,37]. Since our temperature model is inherently limited by the interpolation that we apply in the few gaps in the coverage of the auroral regions the Gemini/TEXES data have, we may be missing the peak in auroral temperatures that could account at least partially for the excess of HCN emission seen interior of the southern oval. However, there is no profile with increased temperatures in the sub-mbar region that enables the reproduction of the observations without invoking a change in the HCN vertical profile. The HCN line is not optically thick and even increasing the sub-mbar temperatures from 170° to 210 K decreases the sub-mbar HCN mole fraction only by roughly 20%, and it still fails to properly fit the line. There is thus a roughly ten times higher abundance of HCN at sub-mbar pressures interior of the southern aurora compared to the surrounding polar region. Observations and models have demonstrated that HCN can be formed by ion-neutral chemistry under auroral-like conditions in Titan's N_2–CH_4 atmosphere (for example, refs. 38,39). Perrin et al.[30] found evidence that HCN formed under such conditions does not bond on organic aerosols (as discussed previously) until small primary monomers have coagulated into large 100 nm-sized monomers. We propose that HCN is formed similarly in Jupiter's auroras and that the source of nitrogen is molecular N_2 quenched at kbar pressures from the thermochemical equilibrium between NH_3 and N_2. Thermochemical model results from ref. 40 indicate that N is roughly four times the protosolar in the deep atmosphere, which produces roughly 10^{-5} of N_2 in the upper troposphere. This N_2 is transported at all latitudes up to its homopause, which resides at 0.1–1 µbar. It is only ionized in the auroras by magnetospheric electrons, which peak in the 10 nbar to 0.1 mbar range (refs. 25,26), to produce HCN. This excess of HCN only produced in the jovian auroras would not contaminate other regions of the planet. Indeed, it would remain confined inside the aurora by the auroral winds observed by Cavalié et al.[21], at least down to pressures where it would be removed by the aerosols. It remains to be shown by chemistry models that this scenario is valid and that there is a chemical pathway to produce roughly 10 ppb of HCN at pressures lower than 10 µbar in the auroras (and not elsewhere on the planet) essentially from the ionization (and subsequent dissociation) of N_2 coming from the interior by energetic electrons precipitating from the Jovian magnetosphere.

These results shed new light on the coupling between magnetospheres and atmospheres in giant planets. New disc-resolved observations of CO_2 with the James Webb Space Telescope[41], possibly coordinated with ALMA mapping observations of CO, HCN and H_2O, as well as dedicated chemical modelling of Jupiter's auroral regions, would certainly help consolidate our findings.

Methods

Observations

We use the observations of Jupiter, performed with ALMA on 22 March 2017, as part of the 2016.1.01235.S project, which have enabled mapping the winds in Jupiter's stratosphere[21]. The rather short integration time of 24 min limits the longitudinal smearing to 15°. The sub-observer latitude of −3° ensures that only the northernmost latitudes were unobserved.

The planet was mapped with 42 antennas using 39-point mosaic (Supplementary Fig. 1), because of its 43.82′ angular size. With the C-1 compact antenna configuration, the resulting elliptical synthetic beam was 1.2′ (East–West) × 1′ (North–South) and the maximum recoverable scale was roughly 8′. Jupiter's disc is thus fully resolved, with a latitudinal resolution of 2° at low latitudes and increasing to 8° at the highest latitudes along the limb. The spectral setup simultaneously covered the HCN (4-3) and CO (3-2) lines at 354.505 and 345.796 GHz,

respectively, with spectral resolutions of 122 and 488 kHz, respectively. Such a high spectral resolution enables fully resolving the lineshape of the HCN and CO lines, which have full-widths at half-maximum in the range of 2–10 MHz. It is thus possible to determine the vertical profile of the observed species, as detailed in the Methods.

Cavalié et al.[21] reduced the data using CASA 4.7.2 and applied bandpass, amplitude and phase calibration using the following sources: J1256-0547 (3C279), Ganymede and J1312-0424, respectively. The calibration uncertainties are roughly 5%. The noise in the observations is at the level of 3–4%.

The continuum is then subtracted in the UV plane to enable imaging the spectral line. This is done using a uniform continuum model. Since we only used the shallow-sounding channels of TEXES, we did not retrieve tropospheric temperatures and cannot produce a more realistic continuum map. This results in an imperfect continuum subtraction, which leaves some continuum residuals. These eventually affect the line-to-continuum ratio and the retrieved mole fraction. For example, in a continuum bright region, that is, with a continuum excess with respect to a uniform disc, the line-to-continuum ratio will be artificially lower and will result in a lower mole fraction. The resulting uncertainty on the column densities is about 30% and is the biggest source of uncertainty in this study.

The final Jupiter spectral images show HCN and CO emission concentrated at the planet limb. This is caused by the increase of the path length through the atmosphere, which induces limb-darkening in the continuum and limb-brightening in the spectral line. We took the 557 HCN spectra and 540 CO spectra they extracted from the limb (at the 1-bar level) to carry out our analyses. The beam was oversampled by a factor of four to five and the spectra were obtained from a bilinear interpolation of the spatial pixels of the data cube. Since the angular resolution is slightly better in the HCN data, we extracted slightly more spectra from this data cube.

Spatial distribution retrieval method

We analysed each CO and HCN limb spectrum with a model that enabled us to retrieve their vertical profiles all along the limb. This model is composed of a forward radiative transfer model and an iterative retrieval algorithm relying on a three-parameter function for vertical profile parametrization. We detail these two components hereafter.

Forward model

Radiative transfer. We used the radiative transfer model described in ref. 42 adapted to Jupiter's atmosphere. It accounts for the three-dimensional (3D) ellipsoidal geometry of the planet. We take the ephemeris from the Jet Propulsion Laboratory (JPL) Horizons Solar System Dynamics ephemerides (https://ssd.jpl.nasa.gov/horizons/) to have the planet geometrical data at the time of the observations. In particular, we use the equatorial angular diameter, the observer sub-latitude and sub-longitude, north pole angle and geocentric distance.

The spectroscopic data for both lines come from the JPL catalogue. We adopted a pressure broadening coefficient γ of 0.145 cm^{-1} atm^{-1} and a temperature dependence exponent n of 0.75 for the HCN line according to ref. 43. For the CO line, we took $\gamma = 0.067$ cm^{-1} atm^{-1} and $n = 0.60$, according to ref. 44.

The continuum is formed from the collision-induced absorption of H_2–He–CH_4 (refs. 45–47) and the far wings of NH_3 and PH_3 lines. We parametrize the vertical profile of both species using $q = q_0 \left(\frac{p}{p_0}\right)^{(1-f)/f}$ with deep mole fractions q_0 of 2×10^{-4} and 6×10^{-7}, cut-off pressures p_0 of 800 and 500 mbar and fractional scale heights f of 0.15 and 0.2 for NH_3 and for PH_3, respectively.

Temperature field. The temperature vertical profile in the stratosphere of Jupiter shows meridional, and (to a smaller extent) zonal variability over the course of only a few weeks in several regions such

as the equatorial and auroral regions (for example, refs. [48],[49]). Fortunately, Jupiter's stratospheric temperatures have been retrieved from Gemini/TEXES observations of the CH_4 band at 7.8 μm a few days before our observations. The TEXES observations record high resolution spectra in 4–6 cm^{-1} wide bands centred at 587, 730, 819, 950 and 1,248 cm^{-1}. The temperatures are retrieved from the 587 and 1,248 cm^{-1} settings, which collectively sound 50 mbar to 1 μbar, as shown with vertical functional derivatives in Fig. 3 in ref. [31]. Upper tropospheric temperatures are only constrained at 100 mbar but not deeper because we did not use the deeper-sounding channels of TEXES in our retrievals. The effect on our abundance retrievals remains insignificant compared to other uncertainty sources. The spectral maps of the equatorial zone up to the mid-latitudes were obtained on 14, 16 and 20 March 2017 by ref. [22] and for the high latitudes on 17–19 March 2017, by ref. [23]. The angular resolution of the observations was diffraction-limited to roughly 0.7′ at 7.8 μm, where the CH_4 emissions were inverted to derive the stratospheric temperature profile, with peak sensitivities between 1 μbar and 50 mbar. For instance, the angular resolution corresponds to a latitude−longitude footprint of roughly 5° at 60° N, which is of the same order as that of the ALMA observations. We reconstructed a full 3D temperature field from the combined retrieved temperature maps, and filled the latitudinal and longitudinal gaps by interpolating linearly between the data points. This results in some discrete jumps such as those seen at 61° N and 66° S, which nonetheless result from the marked boundaries of auroral heating. To speed up the retrievals, we used two-dimensional (2D) latitude and pressure maps instead of the full 3D temperature field. We extracted these 2D thermal maps from the 3D field at 350° W (eastern limb) and 170 W (western limb). They are displayed in Extended Data Fig. 1 and account for the 15° longitudinal smearing of the observations. Note that the heating caused by the northern and southern auroras can be seen on the 170 and 350° W plots, respectively. Cooling in the troposphere and lower stratosphere poleward of roughly 60° is also present. It modifies the local continuum, but barely affects the line amplitude (effect less than 5%). It thus has negligible effects on the retrieved abundances. In a first and simple approach, we do not consider the temperatures at other longitudes in our radiative transfer calculations and essentially work with 2D fields (pressure–latitude) for each limb.

Retrieval model

With known temperature and pressure fields, we used the ALMA observations to obtain vertical profiles of volume mixing ratio of HCN and CO. Using a simple two-parameter profile parametrization with a mixing ratio above a pressure cut-off level would be insufficient to properly fit the HCN lines, especially in the near-continuum wings of the line. We thus opted for a three-parameter parametrization of the vertical profiles, because the HCN line profile clearly indicates a cut-off altitude that has to be described by two parameters (slope of decay and altitude where the decay begins). The mixing ratio as a function of height in km above the 1 bar level, $f(z)$, is parameterized with three independent numbers, a_1, a_2, a_3 as follows:

$$f(z) = a_1 \left[1 + \tanh (z - a_2)/a_3 \right]$$

The inverse problem is then to find only three numbers at each of the limb spectra, where a_1 is the high altitude asymptotical constant mixing ratio above a transition level, a_2 is the altitude of this transition level and a_3 is a scale height informing how quickly the mixing ratio decreases below the transition level with decreasing altitude.

The choice of this parametrization provides several advantages worth pointing out. With only three unknowns the inverse problem is robust and stable, it is relatively fast and it already yields a high quality of fitting (Extended Data Fig. 2), indicating that we exploit most of the information content of the spectra. In addition, the parameterized

vertical profiles capture the key physical behaviour of the actual HCN and CO mixing ratios with cut-off height as a free parameter. We studied the forward radiance Jacobians (as used in inverse problems) and found that the three parameters can be estimated with a high-degree of independence. Also, the stability of the inverse problem indicates no degeneracy between the three parameters.

We solved the inverse problem with an iterative damped least-squares method, also known as Twomey–Tikhonov in Earth atmospheric science literature[50]. The three parameters are assembled into a vector **x**, and the next iteration is obtained as

$$x_{i+1} = x_i + \left(K^T S_e^{-1} K + R \right)^{-1} \left[K^T S_e^{-1} \Delta y - R x_i \right].$$

The Jacobian matrix $K = \frac{\partial y_n}{\partial x_m}$, where y_n is the nth spectral channel of the forward model, was estimated numerically perturbing each of the three parameters by a small amount and recalculating forward model spectra. This matrix remains constant during iterations. The diagonal matrices S_e and $R = \alpha I$ denote random measurement noise $(1 - \sigma)$ and a regularization operator, respectively. K^T is the transpose matrix of K. The regularization parameter, α, was estimated by trial and error with synthetic inversions and then fixed for all subsequent iterations of all retrievals. The Δy term holds differences between measured and calculated spectra for the current estimate of x. The iterative process continues while the current reduced χ_i^2 is smaller than the one from previous iteration within a threshold of 0.5%.

The retrieval process described above requires an initial estimate on the three parameter values for each new observation. For the first inverted spectrum, these were supplied manually on the basis of a few trials. For subsequent points on the map, however, they were taken from the previously inverted measurement before running the first retrieval iteration. This approach is reasonable as we expect adjacent points on the map not to deviate strongly from one another (in mixing ratio). For validation of our assumption, we investigated the spectral line characteristics of adjacent observations. Finally, the least-squares method allowed us to estimate how the random error component in the measurements gets projected into uncertainties in retrieved parameters through the solution covariance matrix. The diagonal elements were used in plotting the retrieved profile uncertainties (as shaded regions in Extended Data Fig. 2) that are generally smaller than 3% on the a_1 parameter, smaller than 1% on the a_2 parameter and in the 5–10% range on the a_3 parameter.

Random samples of retrieved HCN and CO profiles with the corresponding spectra and fit are displayed in Extended Data Fig. 2. About 95% of HCN retrievals converge automatically to the set criteria, and about 98% in case of CO, which is more optically thin. In the few cases that did not automatically converge, we supplied manually a better initial value of the a_2 parameter that allowed the inverse problem to proceed nominally to convergence. The full set of HCN and CO vertical profiles, as retrieved from the data, is displayed in Extended Data Fig. 3 using the same colour code as in Fig. 2 for the various latitude bins.

In addition, we investigated the role of the full 3D temperature field on the mixing ratio retrievals, especially at auroral latitudes where sharp gradients may exist. We compared forward radiative calculations of the limb emission using the retrieved volume mixing ratios and lines of sight going through the full 3D temperature field, with calculations using the same abundance profiles and the 2D temperature maps produced for the two limbs (Extended Data Fig. 1). In most cases, the 3D temperatures did not play any role. However, in a few cases, we identified a need to consider the full 3D inputs in the inversion of the HCN profiles. In these limited cases where the 2D temperatures would produce a fit outside the measurement noise, we reran the retrieval procedure with the full 3D temperature field. These cases represented less than 5% of the HCN spectra and are located at 33° S–46° S and 53° S–57° S on the 350° W limb and 64° S–69° S on the 170 W limb.

Data availability

Observation data can be obtained from the ALMA archive. Temperature profiles, HCN and CO limb spectra and retrieved vertical profiles can be obtained from the following Zenodo repository: https://doi.org/10.5281/zenodo.7928701.

Code availability

Software used for the retrievals is available upon request by contacting the corresponding author.

References

1. Moses, J. I. et al. Photochemistry and diffusion in Jupiter's stratosphere: constraints from ISO observations and comparisons with other planets. *J. Geophys. Res.* **110**, E08001 (2005).
2. Feuchtgruber, H. et al. External supply of oxygen to the atmospheres of the giant planets. *Nature* **389**, 159–162 (1997).
3. Hue, V., Hersant, F., Cavalié, T., Dobrijevic, M. & Sinclair, J. A. Photochemistry, mixing and transport in Jupiter's stratosphere constrained by Cassini. *Icarus* **307**, 106–123 (2018).
4. Harrington, J. et al. in *Jupiter. The Planet, Satellites and Magnetosphere* Vol. 1, 159–184 (eds Bagenal, F. et al.) (Cambridge Univ. Press, 2004).
5. Orton, G. et al. Collision of comet Shoemaker-Levy 9 with Jupiter observed by the NASA Infrared Telescope Facility. *Science* **267**, 1277–1282 (1995).
6. Moreno, R. et al. Jovian stratospheric temperature during the two months following the impacts of comet Shoemaker-Levy 9. *Planet. Space Sci.* **49**, 473–486 (2001).
7. Sánchez-Lavega, A. et al. Motions of the SL9 impact clouds. *Geophys. Res. Lett.* **22**, 1761–1764 (1995).
8. Hammel, H. B. et al. HST imaging of atmospheric phenomena created by the impact of comet Shoemaker-Levy9. *Science* **267**, 1288–1296 (1995).
9. Lellouch, E. et al. Chemical response of Jupiter's atmosphere following the impact of comet Shoemaker-Levy 9. *Nature* **373**, 592–595 (1995).
10. Marten, A. et al. The collision of comet Shoemaker-Levy 9 with Jupiter: detection and evolution of HCN in the stratosphere of the planet. *Geophys. Res. Lett.* **22**, 1589–1592 (1995).
11. Bjoraker, G. L., Stolovy, S. R., Herter, T. L., Gull, G. E. & Pirger, B. E. Detection of water after the collision of fragments G and K of comet Shoemaker-Levy 9 with Jupiter. *Icarus* **121**, 411–421 (1996).
12. Zahnle, K. Dynamics and chemistry of SL9 plumes. In *The Collision of Comet Shoemaker-Levy 9 and Jupiter* (eds Noll, K. S. et al.) 183–212 (Cambridge University Press, 1996).
13. Lellouch, E. et al. The origin of water vapor and carbon dioxide in Jupiter's stratosphere. *Icarus* **159**, 112–131 (2002).
14. Lellouch, E. et al. Carbon monoxide in Jupiter after the impact of comet Shoemaker-Levy 9. *Planet. Space Sci.* **45**, 1203–1212 (1997).
15. Moreno, R., Marten, A., Matthews, H. E. & Biraud, Y. Long-term evolution of CO, CS and HCN in Jupiter after the impacts of comet Shoemaker-Levy 9. *Planet. Space Sci.* **51**, 591–611 (2003).
16. Griffith, C. A. et al. Thermal infrared imaging spectroscopy of Shoemaker-Levy 9 impact sites: spatial and vertical distributions of NH_3, C_2H_4, and 10-μm dust emission. *Icarus* **128**, 275–293 (1997).
17. Griffith, C. A. et al. Meridional transport of HCN from SL9 impacts on Jupiter. *Icarus* **170**, 58–69 (2004).
18. Lellouch, E. et al. On the HCN and CO_2 abundance and distribution in Jupiter's stratosphere. *Icarus* **184**, 478–497 (2006).
19. Cavalié, T. et al. Observation of water vapor in the stratosphere of Jupiter with the Odin space telescope. *Planet. Space Sci.* **56**, 1573–1584 (2008).
20. Benmahi, B. et al. Monitoring of the evolution of H_2O vapor in the stratosphere of Jupiter over an 18-year period with the Odin space telescope. *Astron. Astrophys.* **641**, A140 (2020).
21. Cavalié, T. et al. First direct measurement of auroral and equatorial jets in the stratosphere of Jupiter. *Astron. Astrophys.* **647**, L8 (2021).
22. Cosentino, R. G. et al. New observations and modeling of Jupiter's quasi-quadrennial oscillation. *J. Geophys. Res. Planets* **122**, 2719–2744 (2017).
23. Sinclair, J. A. et al. A high spatial and spectral resolution study of Jupiter's mid-infrared auroral emissions during a solar wind compression. *Planet. Sci. J.* **4**, 76 (2023).
24. Clarke, J. T. et al. Response of Jupiter's and Saturn's auroral activity to the solar wind. *J. Geophys. Res.* **114**, A05210 (2009).
25. Perry, J. J., Kim, Y. H., Fox, J. L. & Porter, H. S. Chemistry of the Jovian auroral ionosphere. *J. Geophys. Res.* **104**, 16541–16565 (1999).
26. Gérard, J.-C. et al. Mapping the electron energy in Jupiter's aurora: Hubble spectral observations. *J. Geophys. Res.* **119**, 9072–9088 (2014).
27. McKay, C. P. Elemental composition, solubility, and optical properties of Titan's organic haze. *Planet. Space Sci.* **44**, 741–747 (1996).
28. Lara, L.-M., Lellouch, E. & Shematovich, V. Titan's atmospheric haze: the case for HCN incorporation. *Astron. Astrophys.* **341**, 312–317 (1999).
29. Vinatier, S. et al. Vertical abundance profiles of hydrocarbons in Titan's atmosphere at 15 °S and 80 °N retrieved from Cassini/CIRS spectra. *Icarus* **188**, 120–138 (2007).
30. Perrin, Z. et al. An atmospheric origin for HCN-derived polymers on Titan. *Processes* **9**, 965 (2021).
31. Sinclair, J. A. et al. Jupiter's auroral-related stratospheric heating and chemistry II: analysis of IRTF-TEXES spectra measured in December 2004. *Icarus* **300**, 305–326 (2018).
32. Wong, A.-S., Yung, Y. L. & Friedson, A. J. Benzene and haze formation in the polar atmosphere of Jupiter. *Geophys. Res. Lett.* **30**, 1447 (2003).
33. Bézard, B., Drossart, P., Encrenaz, T. & Feuchtgruber, H. Benzene on the giant planets. *Icarus* **154**, 492–500 (2001).
34. Wong, A.-S., Lee, A. Y. T., Yung, Y. L. & Ajello, J. M. Jupiter: aerosol chemistry in the polar atmosphere. *Astrophys. J.* **534**, L215–L217 (2000).
35. Friedson, A. J., Wong, A.-S. & Yung, Y. L. Models for polar haze formation in Jupiter's stratosphere. *Icarus* **158**, 389–400 (2002).
36. Zhang, X., West, R. A., Banfield, D. & Yung, Y. L. Stratospheric aerosols on Jupiter from Cassini observations. *Icarus* **226**, 159–171 (2013).
37. Sinclair, J. A. et al. Jupiter's auroral-related stratospheric heating and chemistry I: analysis of Voyager-IRIS and Cassini-CIRS spectra. *Icarus* **292**, 182–207 (2017).
38. Waite, J. H. et al. The process of tholin formation in Titan's upper atmosphere. *Science* **316**, 870–875 (2007).
39. Dobrijevic, M., Loison, J.-C., Hickson, K. M. & Gronoff, G. 1D-coupled photochemical model of neutrals, cations and anions in the atmosphere of Titan. *Icarus* **268**, 313–339 (2016).
40. Cavalié, T., Lunine, J. I. & Mousis, O. A subsolar oxygen abundance or a radiative region deep in Jupiter revealed by thermochemical modeling. *Nat. Astron.* **7**, 678–683 (2023).
41. Norwood, J. et al. Giant planet observations with the James Webb Space Telescope. *Publ. Astron. Soc. Pac.* **128**, 018005 (2016).
42. Cavalié, T. et al. Herschel map of Saturn's stratospheric water, delivered by the plumes of Enceladus. *Astron. Astrophys.* **630**, A87 (2019).

43. Rohart, F., Derozier, D. & Legrand, J. Foreign gas relaxation of the J=0→1 transition of HC^{15}N. A study of the temperature dependance by coherent transients. *J. Chem. Phys.* **87**, 5794–5803 (1987).

44. Dick, M. J., Drouin, B. J., Crawford, T. J. & Pearson, J. C. Pressure broadening of the J=5←4 transition of carbon monoxide from 17 to 200 K: a new collisional cooling experiment. *J. Quant. Spectr. Rad. Transf.* **110**, 619–638 (2009).

45. Borysow, J., Trafton, L., Frommhold, L. & Birnbaum, G. Modeling of pressure-induced far-infrared absorption spectra of molecular hydrogen pairs. *Astrophys. J.* **296**, 644–654 (1985).

46. Borysow, A. & Frommhold, L. Theoretical collision-induced rototranslational absorption spectra for the outer planets: H$_2$-CH$_4$ pairs. *Astrophys. J.* **304**, 849–865 (1986).

47. Borysow, J., Frommhold, L. & Birnbaum, G. Collision-induced rototranslational absorption spectra of H2-He pairs at temperatures from 40 to 3000 K. *Astrophys. J.* **326**, 509–515 (1988).

48. Flasar, F. M. et al. An intense stratospheric jet on Jupiter. *Nature* **427**, 132–135 (2004).

49. Giles, R. S., Greathouse, T. K., Cosentino, R. G., Orton, G. S. & Lacy, J. H. Vertically-resolved observations of Jupiter's quasi-quadrennial oscillation from 2012 to 2019. *Icarus* **350**, 113905 (2020).

50. Twomey, S. *Introduction to the Mathematics of Inversion in Remote Sensing and Indirect Measurements* 2nd edn (Dower Phoenix, 2002).

Acknowledgements

Author contributions

T.C. and L.R. performed the modelling and data analysis. All authors discussed the results and commented on the manuscript.

Competing interests

The authors declare no competing interests.

Additional information

Extended data is available for this paper at https://doi.org/10.1038/s41550-023-02016-7.

Supplementary information The online version contains supplementary material available at https://doi.org/10.1038/s41550-023-02016-7.

Correspondence and requests for materials should be addressed to T. Cavalié.

Peer review information *Nature Astronomy* thanks Imke de Pater, Conor Nixon and the other, anonymous, reviewer(s) for their contribution to the peer review of this work.
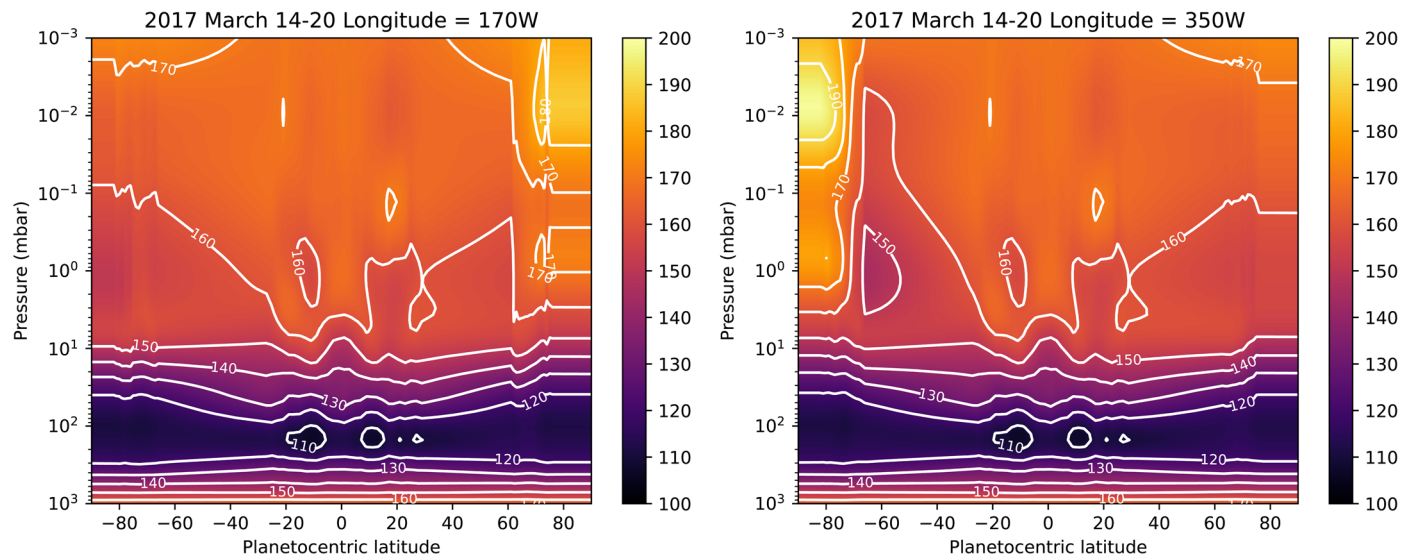
Reprints and permissions information is available at www.nature.com/reprints.

Extended Data Fig. 1 | Temperature fields used in the abundance retrievals. The fields at 170 W (left) and 350 W (right) correspond to the eastern and western limbs, respectively, as reconstructed from the retrievals obtained from Gemini/TEXES observations on March 14–20, 2017.
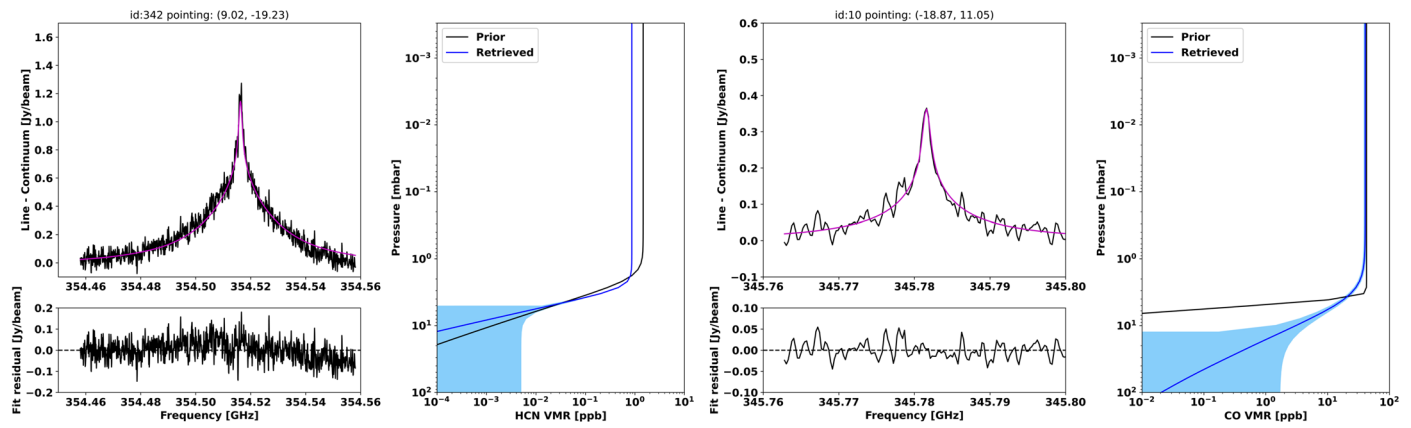
Extended Data Fig. 2 | HCN (left) and CO (right) VMR vertical profile retrieval examples. The a priori and retrieved profiles are shown in black and blue, respectively. The shaded region encompasses the range of 1-σ uncertainties due to random measurement errors. The measurement spectra (black) and fitted spectra (magenta) along with the residuals are shown as well.
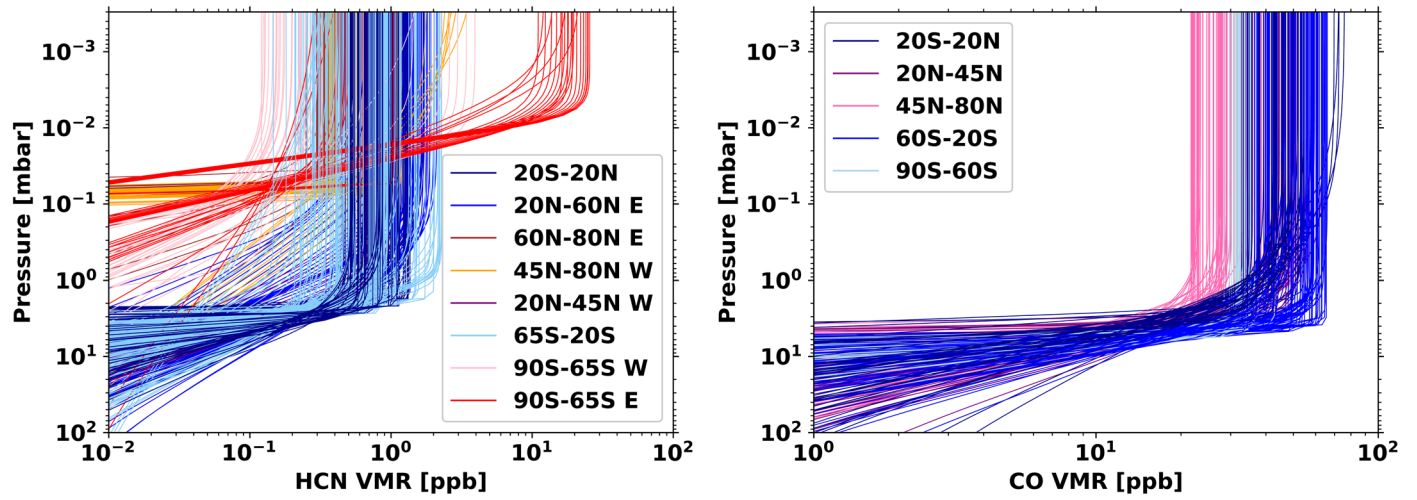
Extended Data Fig. 3 | HCN (left) and CO (right) vertical profiles in Jupiter's stratosphere, as retrieved from the ALMA observations of March 22ⁿᵈ, 2017. They are grouped in latitude bins, similarly to Fig. 2.